ACS Catalysis

Research Article

pubs.acs.org/acscatalysis

Strong Interaction between Pt and Thiolated Carbon for Electrocatalytic Durability Enhancement

Shin-Ae Park, Dae-Suk Kim, Tae-Jun Kim, and Yong-Tae Kim*

School of Mechanical Engineering, Pusan National University, Busan 609-735, Korea

Supporting Information

ABSTRACT: It is widely recognized that the strong metal support interaction (SMSI) can be found between noble metal catalysts and early transition metal oxide supports (e.g., Pt/TiO_2), but not for carbon supports, of which electronic interaction between that and a noble metal is too weak because of the chemical inertness of the surface basal plane. Herein, we report a strong interaction between Pt and carbon through the medium of surface thiol groups. From the in situ XANES studies on the Pt L_3 and the S K absorption edges, it was clearly revealed that the SMSI was formed by the charge back-donation from S to Pt at high potentials, eventually leading to a markedly enhanced tolerance of Pt/S-MWNT against Pt dissolution.

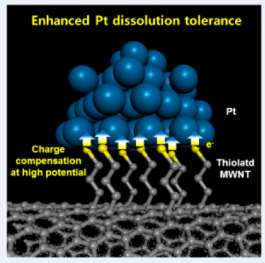

KEYWORDS: *electrocatalysts, SMSI, durability, thiol group, Pt*

1. INTRODUCTION

The durability of Pt-based electrocatalysts is one of the most critical challenges to be addressed in the commercialization of low-temperature fuel cells. The solution to this issue lies in the mitigation of Pt dissolution, particularly at the cathode at high potentials and under acidic conditions.[1] To date, a number of options pertaining to the retardation of Pt dissolution have been reported, including alloying or dealloying,[2,3] core−shell structure,[4] anisotropic structure,[5,6] and the deployment of conducting metal oxide supports resulting in a strong metal support interaction (SMSI).[7] It is widely recognized that SMSI, generally found in noble metal catalysts supported on early transition metal oxides (e.g., Pt/TiO_2), can drastically change the electronic structure by charge transfer, thereby affecting the activity and durability of the catalyst.[8−11] On the contrary, SMSI between metal nanoparticles and carbon supports has not been reported yet. Apparently, it is impossible to induce SMSI with a carbon support because its basal plane is too inert to have an electronic interaction with metal nanoparticles.

Herein, we report a strong interaction formed between Pt nanoparticles and thiolated carbon supports, resulting in markedly enhanced tolerance against Pt dissolution at high potentials. To date, we have investigated various roles of surface thiol groups introduced onto carbon nanotube supports for electrocatalysts. These roles include an effective ligand to stabilize the Pt metal single atoms as an ultimate limit of high dispersion,[12] a mediator to control the size of the Pt nanoparticles,[13] an anchor to impede the agglomeration of Pt nanoparticles,[14] and a controller of the release of metal atoms to prepare a core−shell structure with different release times.[15] Recently, we found another unique effect of surface thiol groups; as shown in Scheme 1, the charge transfer from the surface thiol groups to Pt nanoparticles at high potentials resulted in enhanced durability due to an effective mitigation of Pt dissolution. This finding was made through in situ XANES studies using carefully designed, lab-made measurement cells, and the results were finally verified using first-principle DFT calculations with a plane-wave basis and pseudopotential.

Scheme 1. Charge Compensation of Pt Electrocatalysts by Sulfur Atoms in Surface Thiol Groups on Carbon Nanotube Supports

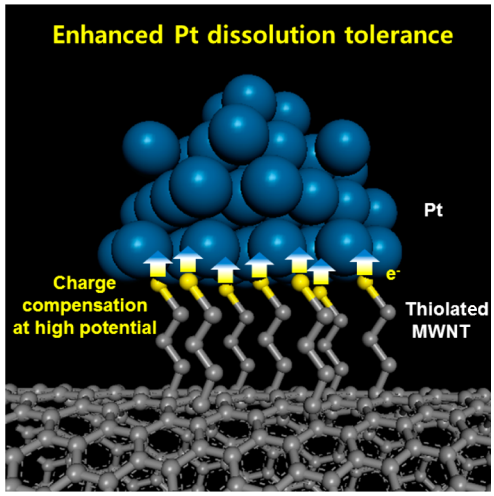

All the samples used in this work were synthesized using the methods described in our previous studies.[12−15] To determine the difference in charge transfer with various surface functional groups, we employed three kinds of representative functional groups, such as thiol, amine, and carboxyl. The thiol and amine groups were introduced by covalent functionalization without any defect formation, whereas the surface carboxyl groups were

Received: August 6, 2013
Revised: October 21, 2013
Published: October 25, 2013

introduced by defect functionalization in a strong acid environment (see Supporting Information). In this paper, we denoted Pt nanoparticles supported on thiol, amine, carboxyl, and nonfunctionalized multiwalled carbon nanotubes by Pt/S-MWNT, Pt/N-MWNT, Pt/O-MWNT, and Pt/MWNT respectively. In addition, a commercially available electrocatalyst (Pt/C, Premetek) was used as a reference sample for comparison purposes. We then proceeded to investigate the variation in charge transfer between Pt and each carbon (Pt/C), nitrogen (Pt/N-MWNT), oxygen (Pt/O-MWNT), and sulfur (Pt/S-MWNT). In particular, we adopted an extremely high loading of Pt (60 wt %) for all the samples to maximize the difference in the Pt dissolution before and after the accelerated durability test (ADT).

2. EXPERIMENTAL SECTION

Synthesis. Multiwalled nanotubes (MWNTs) prepared by a conventional chemical vapor deposition method were purchased from Hanwha Nanotech, Korea. As a purification step, raw soot containing MWNTs was heated for 2 h at 400 °C in static air and subsequently treated with 6 M hydrochloric acid at 70 °C for 12 h. Functionalization of the MWNTs was conducted by a one-step method based on organic peroxides, as reported previously.[16−19] This method, which is nondestructive to the basal plane, utilizes the succinic acid acyl peroxides, $HOOC(CH_2)_2C(O)OO(O)C(CH_2)_2COOH$, as precursors for the functional radicals. To prepare succinic acid acyl peroxides, 10 g of succinic anhydride fine powder (Aldrich) was added to 20 mL of ice cold 8% hydrogen peroxide and stirred for 30 min until all of the powder dissolved and a white solution formed. The solution was filtered and dried for 30 min, after which the succinic acid acyl peroxides were obtained. Purified MWNTs were placed in 50 mL of dry *o*-dichlorobenzene (Aldrich), sonicated for 30 min, and heated at 80 °C for 10 days, with 0.5 g of the succinic acid acyl peroxide added each day. After the reaction was complete, carboxyethyl-radical-functionalized MWNTs were obtained. They were chlorinated by heating at reflux for 12 h with $SOCl_2$ (Wako) at 70 °C. Any remaining $SOCl_2$ was evaporated, then thiolated and aminated MWNTs (S-MWNTs and N-MWNTs) were obtained by reaction with $NH_2(CH_2)_2SH$ (Wako) and $NH_2(CH_2)_2NH_2$ (Wako) in dehydrated toluene (Aldrich) for 24 h at 70 °C, respectively.

The carboxylated MWNT was prepared by simple reflux in H_2SO_4/HNO_3 (3/1 v/v, 98% and 70%, respectively), followed by HCl treatment. For the preparation of Pt nanoparticle-supported various MWNTs, at first, MWNTs (20 mg) were dispersed by sonication in 60 mL of deionized water. After sonication, 9.375 mL of 10 mM $H_2[PtCl_6]$ (Aldrich), equivalent to a 60% weight ratio of Pt to carbon, was dissolved in the above solution with stirring for 2 h. The Pt precursor was simultaneously reduced and supported on the carbon support by using $NaBH_4$ (Aldrich) with vigorous stirring for 12 h. The precipitate was filtered and washed several times with deionized (DI) water and ethanol and dried overnight in a vacuum oven at 50 °C. After evaporation and drying, we obtained 60 wt % Pt supported on purified, thiolated, aminated, and carboxylated MWNTs, referred to as Pt/MWNT, Pt/S-MWNT, Pt/N-MWNT, and Pt/O-MWNT, respectively. The commercial Pt/C (60%, Premetek) was employed for comparison with the prepared samples.

Characterization. The morphology of the electrocatalyst samples was investigated by using transmission electron microscopy (TEM, JEOL JEM-2100F). Specimens for TEM observation were prepared by placing a drop of the particle-dispersed solution onto a copper grid, then the TEM was operated at an accelerating voltage of 200 kV. All the images were recorded with a charge-coupled device camera.

With the synthesized powders, X-ray diffraction (XRD) experiments were carried out with a Philips Pan analytical X-ray diffractometer using Cu Kα radiation (λ = 0.15406 nm). The XRD spectra were obtained at high resolution in the step-scanning mode with a counting time of 5 s per 0.03°. Scans were recorded in the 2θ range 30−90°. Scherrer's equation was used to estimate the particle size from the XRD results. For this purpose, the (111) peak of the Pt face-centered cubic (FCC) structure at 2θ = 40° was selected.

The Pt weight percentage in the catalysts was determined by inductively coupled plasma atomic emission spectrometry (ICP-AES) after preprocessing the Pt/C samples with hydrochloric acid and nitric acid treatments by heating at 300 °C for 3 h. For all the samples, it was found that an ∼60% weight ratio of Pt was successfully loaded on the carbon supports.

XAS spectra were recorded on the BL3C1 and BL7C1 beamline of PLS with a ring current of 120−170 mA at 2.5 GeV. A Si(111) double-crystal monochromator was employed to monochromatize the X-ray photon energy with a homemade in situ measurement cell, as shown in Supporting Information Figure S7. The data were collected in transmission mode with He and N_2 gas-filled ionization chambers as detectors. Higher-order harmonic contamination was eliminated by detuning to reduce the incident X-ray intensity by ∼40%. Energy calibration was completed using standard Pt foil. Every experiment on Pt/C electrocatalysts was conducted using a homemade measurement cell with an aluminum holder for the XAS powder experiments. The in situ X-ray absorption near-edge spectroscopy (XANES) data were recorded using a potentiostat (Biologic VSP) with the application of potential steps in N2-saturated 0.1 M $HClO_4$ solutions. All the spectra were recorded at room temperature. The spectra were processed using the program IFEFFIT[20−23] (version 1.2.11, IFEFFIT, Copyright 2008, Matthew Newville, University of Chicago, http://cars9.uchicago.edu/ifeffit/) with background subtraction (AUTOBK)[24] and normalization.

Computational Methods. First-principle calculations of total energy and electronic structure were performed using CASTEP,[25,26] which is a plane-wave, pseudopotential program based on density functional theory (DFT), working under the local density approximation (LDA). Ion−electron interactions were modeled by a nonlocal real-space,[27] ultrasoft pseudopotential.[28] These models were constructed within a 3D triclinic supercell with lattice constants of *a*, *b*, and *c*. The lattice constants *a*, *b*, and *c* were set to 9.834, 9.834, and 24 Å, respectively, to avoid interactions between Pt nanoparticles. Ten atoms of Pt were chosen for the Pt nanoparticle on the two graphite sheets for the MWNTs. As a comparison of the partial density of states (PDOS) of the Pt d-band, Pt/S-MWNTs and Pt/MWNTs were modeled using Mulliken population analysis. The PDOS of the S d-band was also compared before and after placing the Pt nanoparticle on the Pt/S-MWNT. A plane-wave cutoff of 300 eV was used to ensure convergence in the geometry optimization and PDOS calculations.

Electrochemical Analyses. All electrochemical measurements were performed in a three-electrode electrochemical cell on a potentiostat (Biologic VSP) at room temperature. A glassy carbon electrode (5 mm in diameter) was used as the working

electrode; this was polished with diamond solution and Al_2O_3 slurries and then washed in DI water with sonication before the experiments. Pt/S-MWNT powder (2.5 mg) was dispersed well in DI water (2 mL) using an ultrasonicator, and the dispersion was deposited onto the glassy carbon electrode by dropping 20 μL with a micropipet. Uniform, thin Pt/S-MWNT films were prepared by evaporating the water at room temperature. Nafion solution (0.025 wt %, 20 μL) was dropped onto a suspension-dried glassy carbon electrode and dried in a vacuum oven at 70 °C for 30 min. A platinum wire and a silver chloride electrode (Ag/AgCl sat. 3.5 M KCl) were used as the counter and reference electrodes, respectively. The Ag/AgCl reference electrode was calibrated on a daily basis using a Pt disk electrode and H_2-saturated 0.1 M $HClO_4$ electrolyte to ensure that its potential did not drift. All potentials were converted to the reversible hydrogen electrode (RHE) scale. Cyclic voltammetry (CV) measurements were performed in O_2-free 0.1 M $HClO_4$ electrolyte, obtained by bubbling high-purity N_2 gas for 1 h. The electrodes were cycled in the potential range between 0.05 and 1.15 V vs RHE at a scan rate of 20 mV/s after electrochemical cleaning with a quick scan (scan rate: 200 mV/s) for 50 cycles. After the CV measurements, the oxygen reduction reaction (ORR) was subsequently performed in the same potential range in oxygen-saturated 0.1 M $HClO_4$ at a scan rate of 5 mV/s, with rotation speeds of 100, 400, 900, 1600, and 2500 rpm. The durability tests were carried out at room temperature in O_2-saturated 0.1 M $HClO_4$ solutions, with a cyclic potential sweep between 0.6 and 1.1 V (vs RHE) at a sweep rate of 50 mV/s for 4000 cycles,[4] and then CV measurements were performed in N_2-saturated 0.1 M $HClO_4$ electrolyte in the potential range between 0.05 and 1.15 V (vs RHE) at a scan rate of 20 mV/s. Pt/C Premetek samples were used for the same sets of electrochemical measurements under the same conditions. All the current densities were normalized to the geometric area of the rotating disk electrode, and all electrochemical measurements were carried out at room temperature.

3. RESULTS AND DISCUSSION

The resulting Pt/S-MWNT electrocatalysts were highly dispersed and uniformly size-controlled but showed a slightly higher particle size in comparison with the commercial Pt/C samples. On the other hand, Pt/N-MWNT and Pt/O-MWNT showed a broad particle size distribution that was not well controlled, implying that the amine and carboxyl groups were less effective in the dispersion of Pt nanoparticles as a result of weak interactions. (see Supporting Information Figure S1 and S2) It is well-known that a high dispersion of Pt nanoparticles on carbon nanotube supports is quite difficult because of their inert surfaces.[29,30] However, the particle size and distribution of Pt/S-MWNT was clearly different from that of Pt/N-MWNT or Pt/O-MWNT, but rather close to that of commercial Pt/C. This is because the commercial Pt/C is supported on Vulcan XC-72, which has a favorable porous structure for high dispersion. Actually, in our previous papers,[12−15] it was clearly confirmed from EXAFS and XPS studies that the surface thiol groups act as anchors during the formation of Pt nanoparticles and effectively prohibit their agglomeration by strongly interacting with them. On the other hand, we could not finally confirm the formation of the Pt−N or Pt−O bond, even though we carried out further studies (not shown here). Hence, in this paper, Pt/N-MWNT or Pt/O-MWNT represents not the Pt directly attached to the functional groups such as Pt/S-MWNT, but merely the Pt supported on amine- or carboxyl-functionalized carbon supports. Even though we cannot guarantee the Pt−N or Pt−O bond formation, it is likely that there should be an interaction between them, albeit not so strong. This is because the dispersion of Pt in Pt/N-MWNT or Pt/O-MWNT was obviously higher than that in Pt/MWNT. The reflection peaks in X-ray diffraction (XRD) measurements as shown in Figure 1 were indexed as 111, 200, 220, 311, 222,

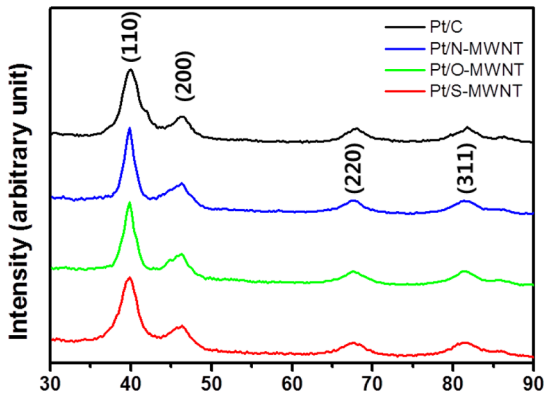

Figure 1. XRD patterns for the Pt peak. The reflection peaks, indexed with 111, 200, 220, 311, and 222, corresponded to face-centered cubic Pt (PDF standard cards, JCPDS 10-1311, space group *Fm*3*m* [225]), respectively.

331, and 420, corresponding to a face-centered cubic Pt with a lattice constant of 3.930 Å (PDF standard cards, JCPDS 10-1311, space group *Fm*3*m* [225]). This confirmed the successful formation of Pt nanoparticles. In addition, the Pt particle size calculated by the Scherrer equation was very consistent with the TEM results: the calculated sizes were 3.3, 4.4, 5.5, and 6.6 nm for Pt/C, Pt/S-MWNT, Pt/N-MWNT, and Pt/O-MWNT, respectively.

First, the activity and durability of ORR were measured using a thin-film rotating disk electrode (TF-RDE) technique[31] and ADT involving fast "potential cycling", respectively. As shown in Figure 2a, the order of ORR activity before ADT was as follows: Pt/C > Pt/S-MWNT ≫ Pt/O-MWNT ≈ Pt/N-MWNT ≈ Pt/MWNT. This outcome was in good agreement with the above-mentioned particle size distribution, which reflected the difference in the degree of interaction of various functional groups with Pt. Even though the onset potential for ORR for Pt/S-MWNT was either similar to or slightly higher than that for Pt/C, the current density for Pt/S-MWNT gradually decreased with a negative potential sweep and eventually went lower than that for Pt/C. As is well-known, the electronic conductivity of carbon nanotubes is much higher than that of carbon black.[32,33] This explains the increased ohmic resistance due to the introduction of surface thiol groups on carbon nanotubes that are highly insulating in nature and through which the electrons must be transferred by the quantum mechanical tunneling mode. This mechanism supports the hypothesis that the slope in the ohmic loss region for Pt/MWNT, where Pt is directly attached to carbon, is similar to that for Pt/C. In the case of Pt/O-MWNT, the ohmic loss was similar to that of Pt/S-MWNT or Pt/N-MWNT, even though the carboxyl group introduced by defect functionalization was much shorter than the thiol or amine groups generated from direct covalent functionalization with a relatively longer succinic acid and amino ethyl chain. Hence, this indicates that

dx.doi.org/10.1021/cs400649n | ACS Catal. 2013, 3, 3067−3074

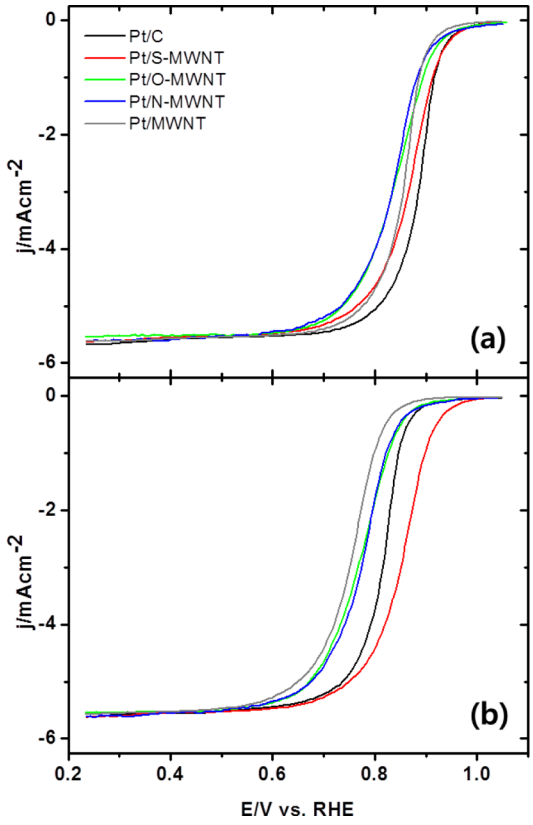

Figure 2. Linear sweep voltammograms (*iR*-free) on various Pt electrocatalysts: (a) before and (b) after 4000 cycles in oxygen-saturated 0.1 M $HClO_4$ at a rotation speed of 1600 rpm, scan rate of 50 mV/s, and room temperature.

the surface of O-MWNT was substantially damaged by defect functionalization involving a strong acid treatment.

It was, however, interesting to note that a marked change in the order of ORR activity was observed after ADT. As shown in Figure 2b, the order of the onset potential for ORR was rearranged as follows: Pt/S-MWNT ≫ Pt/C > Pt/O-MWNT ≈ Pt/N-MWNT > Pt/MWNT. This implies that the durability of Pt/S-MWNT was far superior to other samples. Even though the higher ohmic loss of Pt/S-MWNT was still observed in comparison with Pt/C, almost no deterioration in the onset potential was found before and after ADT. On the contrary, the onset potential for Pt/C considerably decreased, by almost 100 mV, and became rather close to that of Pt/N-MWNT or Pt/O-MWNT after the tests. In particular, the deterioration of Pt/MWNT was substantial. This was attributable to the fact that Pt nanoparticles on the flat basal plane of MWNT readily drifted and agglomerated,[34] whereas the thiol, amine, and carboxyl functional groups on MWNT and the numerous pores of Vulcan XC-72 mitigated agglomeration to a certain extent. Figure 3 exhibits the change in the CV pattern and ORR polarization curve before and after ADT for each sample. One can see that the durability of Pt/S-MWNT is markedly superior to other samples. Because Pt/MWNT did not show any impressive results in ORR activity/durability tests and Pt/C was good enough to show the effect of Pt−C interaction, we excluded Pt/MWNT from the remaining analyses. All the results of electrochemical analyses described above are summarized in Table 1.

It is well-known that Pt dissolution begins at around 0.8 V (vs RHE) and is directly related to the tendency of electron loss (or ionization) at high potentials.[35−38] If such tendency is understood, then the fundamental basis for the results of ADT

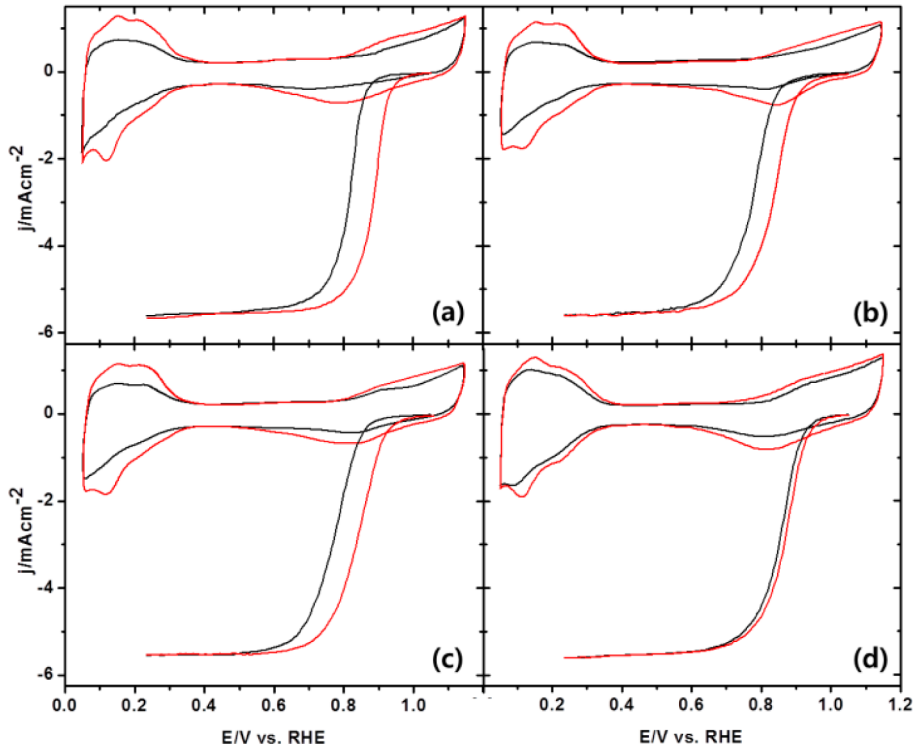

Figure 3. Cyclic and linear sweep voltammograms (*iR*-free) on various Pt electrocatalysts before (red) and after (black) 4000 cycles in oxygen-saturated 0.1 M $HClO_4$ at a rotation speed of 1600 rpm, a scan rate of 50 mV/s, and room temperature for (a) Pt/C, (b) Pt/N-MWNT, (c) Pt/O-MWNT, and (d) Pt/S-MWNT.

dx.doi.org/10.1021/cs400649n | *ACS Catal.* 2013, 3, 3067−3074

Table 1. Onset and Half-Wave Potential, ECSA, and Specific Activities at 0.9 V (versus RHE)

	onset potential (V versus RHE)		half-wave potential (V versus RHE)		ECSA (m^2/g_{Pt})		specific activity[a] ($\mu A/cm^2_{Pt}$)	
catalysts	initial	after ADT	initial	after ADT	initial	after ADT	initial	after ADT
Pt/C	0.98	0.90	0.89	0.81	67.87	38.54	228.47	23.58
Pt/S-MWNT	0.98	0.98	0.87	0.86	58.25	50.11	201.86	165.17
Pt/O-MWNT	0.94	0.88	0.82	0.78	54.38	29.23	123.51	15.83
Pt/N-MWNT	0.94	0.88	0.82	0.78	55.32	28.84	89.63	11.36

[a]The specific activity was calculated by using the current density at 0.9 V (versus RHE) and the obtained ECSA.

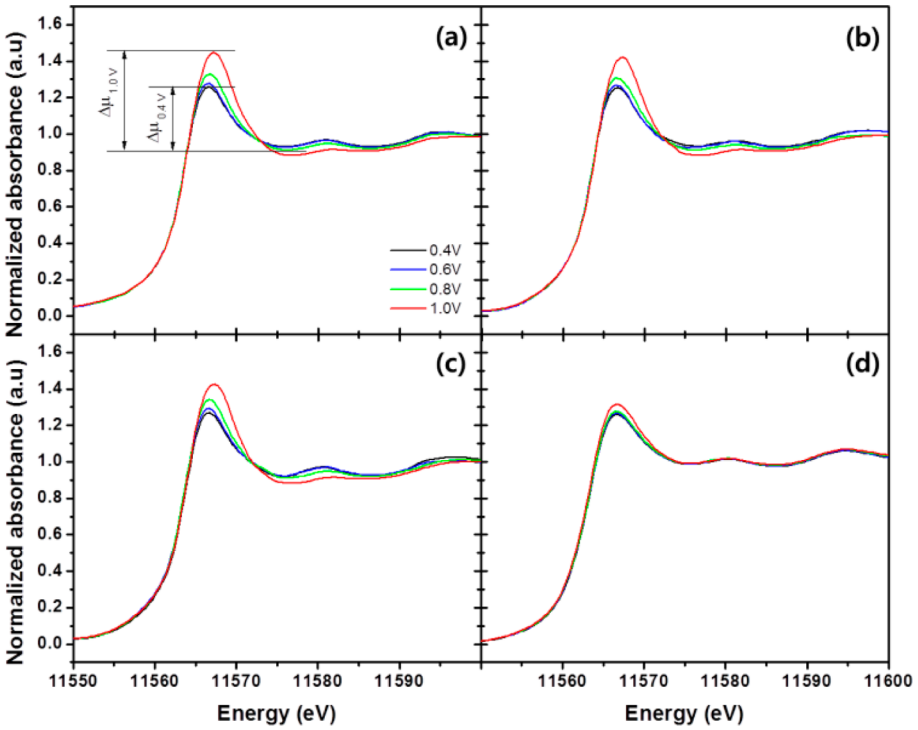

Figure 4. In situ XANES spectra of Pt L_3 absorption edge with potential application on (a) Pt/C, (b) Pt/N-MWNT, (c) Pt/O-MWNT, and (d) Pt/S-MWNT.

can be elucidated. The electron-density change in the metal valence d-band upon the application of a potential was measured by the white line peak in XANES. This peak was formed by the excitation of a core electron to a continuum state in an unoccupied band by X-ray absorption and was therefore directly related to the d-band vacancy. To investigate the electron-density change in the valence d-band at high potentials, we employed in situ XANES measurements. Figure 4 shows the change in the intensity of the white line with increasing potential in the Pt L_3 absorption edge, which corresponds to the electron excitation from the Pt $2p_{3/2}$ orbital to the unoccupied continuum state. It was interesting to note that the degree of increase in the intensity of the white line at high potentials for Pt/S-MWNT was much lower than that for the other samples, as shown Figures 4 and 5, implying that the Pt/S-MWNT had the least tendency of ionization at high potentials. This indicated that Pt/S-MWNT had superior electron-retention properties in comparison with the other samples and, hence, enhanced tolerance against Pt dissolution. Therefore, it can be inferred that the electronic interaction between Pt nanoparticles and thiol groups is much higher than amine or carboxylic groups, and the carbon-basal plane. This could provide a clue to understanding the basis for the enhanced durability of Pt/S-MWNT. The obtained results on

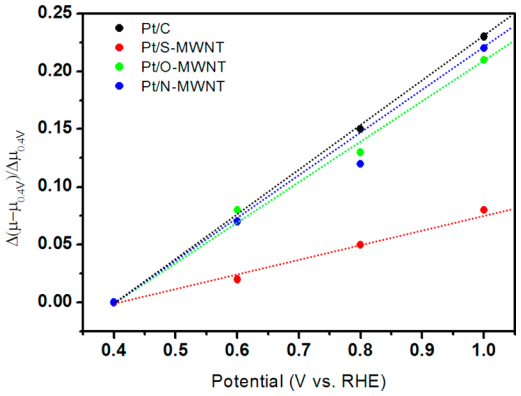

Figure 5. Comparison of the change of the absorption edge peaks of the XANES spectra as a function of potential in 0.1 M $HClO_4$.

the fine structure by data fitting of EXAFS signals to the FEFF 8.3 model are summarized in Supporting Information Table S1.

The above-mentioned observations motivated us to vigorously investigate the change in the valence state of sulfur at high potentials and thereby to employ the in situ XANES measurement on the S K-edge with soft X-ray, which corresponded to the electronic excitation from the 1s orbital

dx.doi.org/10.1021/cs400649n | ACS Catal. 2013, 3, 3067−3074

of S to the unoccupied continuum state. Through this measurement, we confirmed the charge compensation from the sulfur in the thiol groups to the Pt valence d-band at high potentials.

Figure 6 shows the difference in the change of the white line with the application of potential as a function of the presence of

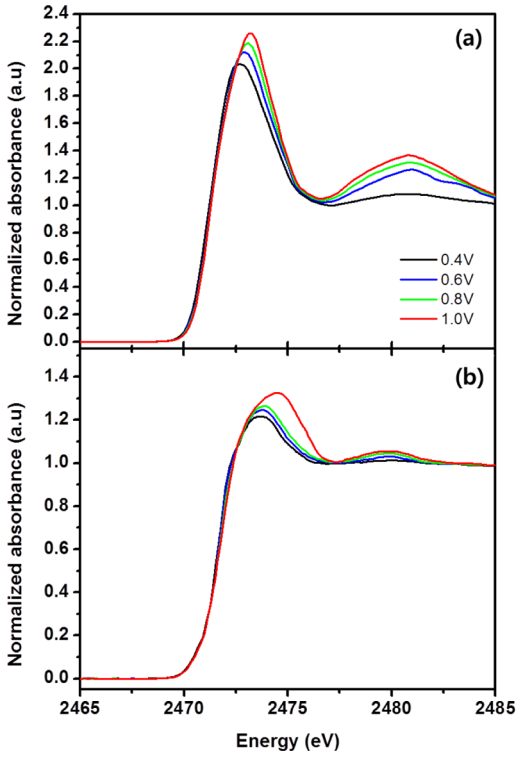

Figure 6. In-situ XANES spectra of the S K absorption edge with potential application on (a) S-MWNT and (b) Pt/S-MWNT.

Pt on the thiol groups. First, two major peaks appeared at approximately 2473 and 2480 eV in the absorption patterns corresponding to 1s → σ^* (S−C or S−Pt) and 1s → σ^* (S−O) transitions, respectively.[39,40] We found that the intensity of both peaks increased with increasing applied potential, indicating that the sulfur was gradually oxidized. In addition, the blue shift of the absorption edge with increasing applied potential implied that the covalency of S−C or S−Pt increased as a result of sulfur oxidation. It is noteworthy that while the intensity of the white line in the S K-edge for thiol groups in the absence of Pt (Figure 6a) gradually increased with increasing potential, that for the thiol groups in the presence of Pt (Figure 6b) suddenly spiked at 1.0 V. This was consistent with the change in the intensity of the white line for the Pt L_3-edge, as shown in Figure 4; that is, the increase in the intensity of the white line for Pt/S-MWNT at 1.0 V was much less than the other samples. Hence, the in situ S K-edge XANES data provided strong evidence of charge compensation by the donation of an electron from sulfur to platinum at high potentials where Pt began to dissolve. This phenomenon seemed to be somewhat contrary to the general charge transfer concept in self-assembled monolayers (SAMs) of thiol groups on the Pt surface, wherein the electrons are transferred from Pt to S during SAM formation as follows:[41]

$$RSH + M_n^0 \rightarrow RS^-M^+M_{n-1}^0 + 1/2H_2$$

However, in our study, it was obvious that the electron distribution between Pt and S drastically changed at high potentials (particularly over 1.0 V). In other words, the initially transferred electron from Pt to sulfur during Pt−S bond formation was back-donated to Pt at high potentials, and therefore, Pt dissolution by electron loss was effectively inhibited by the charge compensation from sulfur. This mechanism was verified with the change in the intensity of the white line against application of a potential by using the in situ XANES techniques. Therefore, charge compensation could be the reason behind the inhibition of Pt dissolution and the markedly enhanced electron retention in Pt/S-MWNT.

In addition to the role of surface thiol groups as charge compensators at high potential, another advantageous role for the durability enhancement can be suggested from the TEM images and the size distribution after ADT cycles, as shown in Supporting Information Figures S3 and S4, respectively. It is widely recognized that the particle size increase with cycles can occur by two modes: one is the Ostwald ripening and the other is a simple sintering due to the drafting and collision on the surface.[9,10] In the former case, it was clearly identified that the Ostwald ripening was significantly suppressed because of the electron retention property of Pt/S-MWNT due to the charge compensation at high potential as confirmed with in situ XANES studies. In the latter case, it can be also confirmed that the sintering tolerance of Pt/S-MWNT is superior to that of Pt/C because little change in the particle size distribution was observed from the TEM observation after ADT, as shown in Supporting Information Figure S3. It could be natural that the sintering tolerance for Pt/S-MWNT could be higher than Pt/C

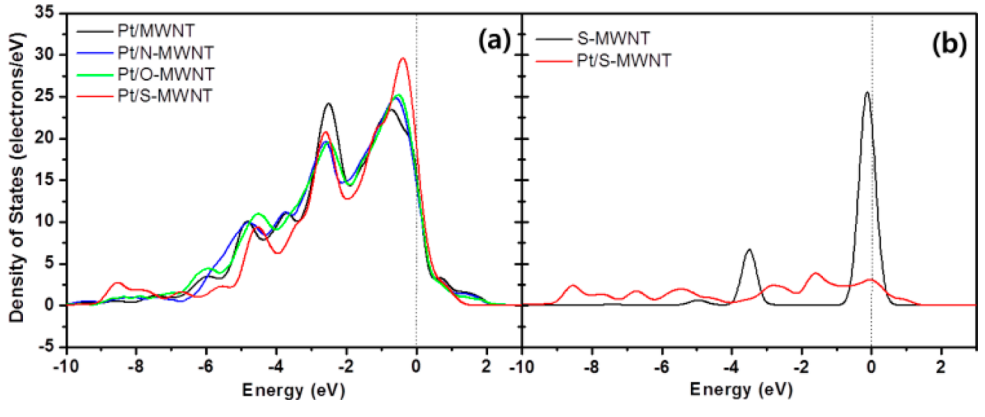

Figure 7. Projected density of state for (a) Pt 5d band and (b) S 3p band calculated by CASTEP code.

dx.doi.org/10.1021/cs400649n | ACS Catal. 2013, 3, 3067−3074

because the surface drifting of the particle for Pt/S-MWNT should be effectively restrained due to the much stronger interaction of Pt with the thiol groups (Pt/S-MWNT) than the basal plane of graphite (Pt/C). Hence, it can be suggested that the surface thiol groups act as both the charge compensators to suppress the dissolution at high potential and the sintering inhibitor to restrain the particle agglomeration.

Such electronic interactions between Pt and sulfur can also be elucidated by using first-principle calculations. Figure 7 shows the projected density of states (PDOS) of both Pt and S calculated with CASTEP,[24,25] a plane-wave, pseudo-potential code based on density functional theory (DFT) and involving local density approximation. The simplified models used for this calculation are shown in Supporting Information Figures S5 and S6. It is worth noting that the PDOS of Pt near the Fermi level (primarily, the Pt 5d band) increased for Pt/S-MWNTs in comparison with Pt on carbon. In the case of S, the PDOS was mainly composed of 3p electrons of S and markedly broadened after the loading of Pt. This indicated that a hybridized Pt 5d−S 3p band was formed, and therefore, the charge compensation by back-donation from the thiol groups to Pt nanoparticles readily occurred at 1.0 V, where the Pt 5d electron near the Fermi level was prone to be lost.

4. CONCLUSIONS

In summary, we reported a strong interaction between Pt nanoparticles and carbon supports through the medium of surface thiol groups. We investigated the effect of electronic interaction between Pt nanoparticles and various functional groups on carbon supports, such as thiol, amine, carboxyl, and carbon basal plane, on the tolerance of Pt dissolution, mainly by using the in situ XANES technique. The strong interaction was found only in Pt/S-MWNT, but little to no effect was exhibited by Pt/N-MWNT, Pt/O-MWNT, and Pt/C. From the in situ XANES studies on the Pt L_3 and S K absorption edges, it was clearly revealed that the basis for the markedly enhanced tolerance of Pt/S-MWNT against Pt dissolution was the charge compensation from S to Pt at high potentials. It was also determined using DFT calculations that the hybridized Pt 5d−S 3p band was formed as a result of a chemical bond, thereby enabling a speedy charge transfer. Hence, we believe that the deployment of surface thiol groups is a promising methodology that can drastically increase the tolerance against Pt dissolution at high potentials and can solve the problem of durability of low-temperature fuel cells.

■ ASSOCIATED CONTENT

Supporting Information

TEM images, particle size distribution, DFT model, XANES spectra of Pt and Au L_3 absorption edges, and lab-made in situ XANES measurement cell design. This material is available free of charge via the Internet at http://pubs.acs.org.

■ AUTHOR INFORMATION

Corresponding Author

*E-mail: yongtae@pusan.ac.kr.

Notes

The authors declare no competing financial interest.

■ ACKNOWLEDGMENTS

This work was supported by the national research foundation of Korea (NRF) grants (NRF-2012R1A1A2007624 and NRF-2012K2A1A2032856), the Korea CCS R&D Center (KCRC) grant (2013M1A8A1040703), and the GCRC-SOP grant funded by the Government of Korea.

■ REFERENCES

(1) Zhang, J.; Sasaki, K.; Sutter, E.; Adzic, R. R. *Science* **2007**, *315*, 220−222.
(2) Stamenkovic, V. R.; Fowler, B.; Mun, B. S.; Wang, G. F.; Ross, P. N.; Lucas, C. A.; Markovic, N. M. *Science* **2007**, *315*, 493−497.
(3) Strasser, P.; Koh, S.; Anniyev, T.; Greeley, J.; More, K.; Yu, C.; Liu, Z.; Kaya, S.; Nordlund, D.; Ogasawara, H.; Toney, M. F.; Nilsson, A. *Nat. Chem.* **2010**, *2*, 454−460.
(4) Stamenkovic, V. R.; Mun, B. S.; Mayrhofer, K. J. J.; Ross, P. N.; Markovic, N. M. *J. Am. Chem. Soc.* **2006**, *128*, 8813−8819.
(5) Lim, B.; Jiang, M.; Camargo, P. H. C.; Cho, E. C.; Tao, J.; Lu, X.; Zhu, Y.; Xia, Y. *Science* **2009**, *324*, 1302−1305.
(6) Chen, Z.; Waje, M.; Li, W.; Yan, Y. *Angew. Chem., Int. Ed.* **2007**, *46*, 4060−4063.
(7) Wang, C.; Waje, M.; Wang, X.; Tang, J. M.; Haddon, R. C.; Yan, Y. *Nano Lett.* **2003**, *4*, 345−348.
(8) Tauster, S. J.; Fung, S. C.; Baker, R. T. K.; Horsley, J. A. *Science* **1981**, *211*, 1121−1125.
(9) Vielstich, W.; Lamm, A.; Gasteiger, H. *Handbook of Fuel Cells: Fundamentals, Technology and Applications*; Wiley: New York, 2003.
(10) Wieckowski, A.; Savinova, E. R.; Vayenas, C. G. *Catalysis and Electrocatalysis at Nanoparticle Surface*; Marcel Dekker: New York, 2003.
(11) Horsley, J. A. *J. Am. Chem. Soc.* **1979**, *101*, 2870−2874.
(12) Kim, Y.-T.; Ohshima, K.; Higashimine, K.; Uruga, T.; Takata, M.; Suematsu, H.; Mitani, T. *Angew. Chem., Int. Ed.* **2006**, *45*, 407−411.
(13) Kim, Y.-T.; Uruga, T.; Mitani, T. *Adv. Mater.* **2006**, *18*, 2634−2638.
(14) Kim, Y.-T.; Mitani, T. *J. Catal.* **2006**, *238*, 394−401.
(15) Kim, Y.-T.; Lee, H.; Kim, H. J.; Lim, T. H. *Chem. Commun.* **2010**, *46*, 2085−2087.
(16) Dujardin, E.; Ebbesen, T. W.; Hiura, H.; Tanigaki, K. *Science* **1994**, *265*, 1850−1852.
(17) Peng, H.; Alemany, L. B.; Margrave, J. L.; Khabashesku, V. N. *J. Am. Chem. Soc.* **2003**, *125*, 15174−15182.
(18) Peng, H.; Reverdy, P.; Khabashesku, V. N.; Margrave, J. L. *Chem. Commun.* **2003**, 362−363.
(19) Ying, Y.; Saini, R. K.; Liang, F.; Sadana, A. K.; Billups, W. E. *Org. Lett.* **2003**, *5*, 1471−1473.
(20) Newville, M. *J. Synchrotron Radiat.* **2001**, *8*, 322−324.
(21) Ravel, B. *J. Synchrotron Radiat.* **2001**, *8*, 314−316.
(22) Ravel, B.; Newville, M. *J. Synchrotron Radiat.* **2005**, *12*, 537−541.
(23) Newville, M. *J. Synchrotron Radiat.* **2001**, *8*, 96−100.
(24) Newville, M.; Līviņš, P.; Yacoby, Y.; Rehr, J. J.; Stern, E. A. *Phys. Rev. B* **1993**, *47*, 14126−14131.
(25) Milman, V.; Winkler, B.; White, J. A.; Pickard, C. J.; Payne, M. C.; Akhmatskaya, E. V.; Nobes, R. H. *Int. J. Quantum Chem.* **2000**, *77*, 895−910.
(26) Payne, M. C.; Teter, M. P.; Allan, D. C.; Arias, T. A.; Joannopoulos, J. D. *Rev. Mod. Phys.* **1992**, *64*, 1045−1097.
(27) Kingsmith, R. D.; Payne, M. C.; Lin, J. S. *Phys. Rev. B* **1991**, *44*, 13063−13066.
(28) Vanderbilt, D. *Phys. Rev. B* **1990**, *41*, 7892−7895.
(29) Jiang, K.; Eitan, A.; Schadler, L. S.; Ajayan, P. M.; Siegel, R. W.; Grobert, N.; Mayne, M.; Reyes-Reyes, M.; Terrones, H.; Terrones, M. *Nano Lett.* **2003**, *3*, 275−277.
(30) Lordi, V.; Yao, N.; Wei, J. *Chem. Mater.* **2001**, *13*, 733−737.
(31) Schmidt, T. J.; Gasteiger, H. A.; Stcob, G. D.; Urban, P. M.; Kolb, D. M.; Behm, R. J. *J. Electrochem. Soc.* **1998**, *145*, 2354−2358.
(32) Sun, X.; Li, R.; Villers, D.; Dodelet, J. P.; Desilets, S. *Chem. Phys. Lett.* **2003**, *379*, 99−104.

(33) Li, Y.; Zhou, W.; Wang, H.; Xie, L.; Liang, Y.; Wei, F.; Idrobo, J.-C.; Pennycook, S. J.; Dai, H. *Nat. Nanotechnol.* **2012**, *7*, 394−400.
(34) Regan, B. C.; Aloni, S.; Ritchie, R. O.; Dahmen, U.; Zettl, A. *Nature* **2004**, *428*, 924−927.
(35) Tseung, A. C. C.; Vassie, P. R. *Electrochim. Acta* **1976**, *21*, 315−318.
(36) Honji, A.; Mori, T.; Tamura, K.; Hishinuma, Y. *J. Electrochem. Soc.* **1988**, *135*, 355−359.
(37) Pourbaix, M. Pourbaix M., Ed.; NACE International, Houston, Texas, 1974; p 644.
(38) Akita, T.; Taniguchi, A.; Maekawa, J.; Sirorna, Z.; Tanaka, K.; Kohyama, M.; Yasuda, K. *J. Power Sources* **2006**, *159*, 461−467.
(39) Zhang, P.; Kim, P. S.; Sham, T. K. *Appl. Phys. Lett.* **2003**, *82*, 1470−1472.
(40) Zhang, P.; Sham, T. K. *Appl. Phys. Lett.* **2003**, *82*, 1778−1780.
(41) Wertheim, G. K.; Dicenzo, S. B.; Youngquist, S. E. *Phys. Rev. Lett.* **1983**, *51*, 2310−2313.